Journal of Neural Engineering

Customizing the human-avatar mapping based on EEG error related potentials during avatar-based interaction.

To cite this article before publication: Fumiaki Iwane *et al* 2024 *J. Neural Eng.* in press https://doi.org/10.1088/1741-2552/ad2c02

Customizing the human-avatar mapping based on EEG error related potentials during avatar-based interaction

Fumiaki Iwane[1,2,3,*], Thibault Porssut[4,5,10,*], Olaf Blanke[5,6], Ricardo Chavarriaga[7,8], José del R. Millán[2,3,7,9] Bruno Herbelin[5,†], & Ronan Boulic[4,†]

[1] Learning Algorithms and Systems Laboratory (LASA), École Polytechnique Féderale de Lausanne (EPFL), 1015 Lausanne, Switzerland
[2] Dept. of Electrical and Computer Engineering, The University of Texas at Austin, Austin, TX 78712, USA
[3] Dept. of Neurology, The University of Texas at Austin, Austin, TX 78712, USA
[4] Immersive Interaction Research Group (IIG), Ecole Polytechnique Fédérale de Lausanne (EPFL), Switzerland
[5] Laboratory of Cognitive Neuroscience (LNCO), Ecole Polytechnique Fédérale de Lausanne (EPFL), Switzerland
[6] Dept. of Neurology, Geneva University Hospitals, Switzerland
[7] École Polytechnique Féderale de Lausanne (EPFL), Campus Biotech, 1202 Genève, Switzerland
[8] Centre for Artificial Intelligence, Zurich University of Applied Sciences (ZHAW), Winterthur, Switzerland
[9] Mulva Clinic for the Neurosciences, The University of Texas at Austin, Austin, TX 78712, USA
[10] Capgemini Engineering, Paris, France
[*] These authors contributed equally to this work.
[†] These authors have equally supervised this work.

E-mail: `fumi.iwane@nih.gov, bruno.herbelin@epfl.ch, ronan.boulic@epfl.ch`

Abstract. *Objective.* A key challenge of virtual reality (VR) applications is to maintain a reliable human-avatar mapping. Users may lose the sense of controlling (sense of agency), owning (sense of body ownership), or being located (sense of self-location) inside the virtual body when they perceive erroneous interaction, i.e. Break-in-embodiment (BiE). However, the way to detect such an inadequate event is currently limited to questionnaires or spontaneous reports from users. The ability to implicitly detect BiE in real-time enables us to adjust human-avatar mapping without interruption. *Approach.* We propose and empirically demonstrate a novel Brain Computer Interface (BCI) approach that monitors the occurrence of BiE based on the users' brain oscillatory activity in real-time to adjust the human-avatar mapping in VR. We collected EEG data of 37 participants while they performed reaching movements with their avatar with different magnitude of distortion. *Main results.* Our BCI approach seamlessly predicts occurrence of BiE in varying magnitude of erroneous interaction. The mapping has been customized by BCI-reinforcement learning (RL) closed-loop system to prevent BiE from occurring. Furthermore, a non-personalized

BCI decoder generalizes to new users, enabling "Plug-and-Play" ErrP-based non-invasive BCI. The proposed VR system allows customization of human-avatar mapping without personalized BCI decoders or spontaneous reports. *Significance.* We anticipate that our newly developed VR-BCI can be useful to maintain an engaging avatar-based interaction and a compelling immersive experience while detecting when users notice a problem and seamlessly correcting it.

1. Introduction

Virtual Reality (VR) systems are becoming widespread in industrial, clinical and training applications for their benefit in ecological validity and physical involvement of participants. One of the main challenges of VR is to provide users with a sense of having a virtual body during immersion in order to interact with the virtual world. The Sense of Embodiment (SoE) for a virtual body representation, the avatar, is a highly subjective experience that must be induced and maintained to support successful interactions in immersive VR [1]. SoE has been described to involve the following components for successful human-avatar mappings: agency, body ownership, and self-location [2]. The disruption of at least one of them causes a Break in Embodiment (BiE), leading to a degradation of the virtual experience [1, 3, 4]. However, the way to detect such an inadequate event is currently limited to explicit feedback from users, e.g. questionnaires or spontaneous reports. Detecting BiE implicitly and in real-time would allow customizing the mapping between users and their avatars so as to fine-tune the interaction possibilities in VR without interruption.

In the 1990s, research on neural processes revealed error-related brain activity in EEG signals originating from the anterior cingulate cortex (ACC) after perception of errors [5, 6]. Holroyd and Coles [7] proposed that an error-processing system in the ACC serves as reinforcement-learning signals to correct errors. Further studies have also shown that error-related potentials (ErrPs) spontaneously arise when users experience BiEs during avatar-based interaction in VR [4, 8, 9, 10, 11, 12, 13]. These findings support the notion of an accumulation of errors in these conditions [14, 15, 16], where cognitive processes in embodiment contribute to a global error in user experience. It is also well established that brain-computer interfaces (BCIs) benefit from real-time ErrP detection to offer intuitive control of external devices without requiring explicit feedback, as instead they can infer participants' perception of errors from their brain activity and adapt accordingly [17, 18, 19, 20, 21, 22]. Some BCIs have succeeded in decoding the presence of ErrPs during continuous interaction [23, 24, 25], with e.g., the possibility to customize robot trajectories for each participant based on continuous ErrP detection [26, 27]. It thus appears that the methods used in ErrP-based BCI provide the adequate approach for continuously and implicitly adjusting the interaction with avatar in immersive VR.

Although recent studies show that ErrP-based BCI allows customization of continuous human-computer interactions, its use is still limited to interactions with

a computer application [25] or a robotic arm [26, 27]. This may in part be due to the need to train personalized decoders, which require a large amount of repetitions and observations before being operational. In our context, this limitation would, however, defeat the purpose of using BCI to implicitly improve interaction in VR as the objective is specifically to avoid repetitively causing BiE, and eventually to use this method in a general immersive VR application context. Hopefully, a recent study demonstrated the feasibility of using the non-personalized decoder with some reductions in decoding performance [24]. However, it remains to be tested if, despite these limitations, non-personalized ErrP decoders can be used in a different way, as in our case for adjusting the mapping between human and avatar actions.

In a previous study, we demonstrated the feasibility of adapting the human-avatar mapping in VR based on the explicit feedback of users [28]. However, it still needs to be demonstrated that it is possible to adjust this human-avatar mapping by implicitly predicting the occurrence of BiE, while avoiding to interrupt the interaction flow and break presence. We hypothesize that real-time detection of ErrPs during avatar-based interaction can predict the occurrence of BiE, and thus allows seamless customization of the mapping. To demonstrate this, we implemented a BCI system that monitors the presence (or absence) of ErrP in real time while distorting the human-avatar mapping in varying magnitudes (Figure 1a, c).

The use of distortion of the human-avatar mapping has been frequently employed in 3D interaction methods, even without haptic feedback [29, 30, 31]. For example, one of the earliest methods focused on enhancing the effectiveness of user interactions by deliberately altering the mapping between real and virtual bodies for a stretching arm. This alteration resulted in an expanded reachable space centered around the user's body [32]. Nevertheless, the challenge lies in fine-tuning of distortion parameters while preventing the occurrence of BiE. For instance, Porssut et al. [1, 33] demonstrated that users tolerate and even prefer distorted mapping with their avatar movement when this helps to accomplish complex movements. However, once distortion surpasses a certain threshold, it can lead to BiE. Specifically, our aim here was thus to customize the human-avatar mapping distortion magnitudes based on implicit ErrP-BCI feedback in order to aid in accomplishing a reaching action while preventing BiEs from occurring. We recorded the EEG signals of participants while they were embodied in a full-body avatar. The participants performed reaching movements to a target while their avatar's reaching movement was distorted in varying magnitudes. We expect ErrPs to appear when participants perceive excessive support from the distortion. The real-time ErrP decoding output was used to identify optimal distortion magnitudes through a reinforcement learning (RL) algorithm. We then further investigated the feasibility of customizing the mapping with the non-personalized ErrP decoder outputs in addition to the use of personalized decoder in both time-locked and continuous classification.

2. Methods

2.1. Participants

37 healthy subjects participated in the study (36 right-handed, 16 females, 23.4±3.5 years [mean±std]). All participants had normal or corrected-to-normal vision and gave their informed consent prior to participation. The study was performed in accordance with the ethical standards as defined in the Declaration of Helsinki and was approved by the Swiss Ethics Committees of the canton of Vaud on research involving humans (project n.2018-01601). Among the 37 subjects, the demographic survey revealed only one person with extensive experience in VR, three with good experience with VR, and ten with no experience while others tried it only a few times.

2.2. Experimental protocol

Experimental environment Participants sat in a comfortable chair and EEG signals were recorded throughout the experiment. The HTC Vive Pro Eye, a Head-Mounted Display (HMD) with 1440 x 1600 pixels per eye, 110 ° field of view and 90 Hz refresh rate, and a 120 Hz eye-tracking system with an accuracy of 0.5-1.1° was used to monitor subjects' eye-movements. Bose QuietComfort 20 in-ear headphones with active noise canceling delivered a non-localized white noise. We captured participants' motion with 8 HTC Vive Trackers V2 (one to indicate the origin of the room in front of the chair where subjects sit, one on the subjects' chest, and three on each shoulder, elbow and hand). The participants also held an HTC Vive controller in their left hand to answer questions (Figure 1a). Figure 1 and a supplementary video illustrate the general study design.

The virtual environment was a square room of $6\times6\times3m^3$ with a chair in the middle. An avatar holding a tennis ball in its right hand was calibrated to co-locate the subjects' body. Haptic feedback was sustained by physically holding a real tennis ball while subjects observed a virtual tennis ball positioned in the same location. This maintained visuo-proprioceptive and tactile coherence between the real and virtual hands. The application was implemented using Unity 3D 2019.2.0f1. The participants' movements were reproduced through animation of the avatar using LimbIk from FinalIK‡.

Experimental procedure We performed the experiment in three groups. 14, 12 and 11 participants were in the first, second, and third groups, respectively. The experimental procedures of the first and second groups were divided into five phases (Figure 1e); calibration, explanation, decoder-calibration, practice and distortion-adaptation. First, the motion capture suit, avatar, and EEG were calibrated (calibration phase). Then the participants performed the six trials with instructions (explanation phase). They then performed four runs of 75 trials, i.e. 50 trials without distortion and 25 trials with distortion (decoder-calibration phase). These data were used to train a personalized

‡ root-motion.com

ErrP decoder. Each run used a different magnitude of distortion in a random order (3,5,7,10, see Section 2.3). The participants performed the same task as in the decoder-calibration phase until convergence of the RL algorithm (distortion-adaptation phase, see Section 2.5 for details). During the distortion-adaptation phase, the personalized decoder predicted the occurrence of BiE to customize the human-avatar mapping. Time-locked and continuous classification was performed during the distortion-adaptation phase for the first and second groups, respectively. In the third group (non-personalized decoder) the experiment was divided into the calibration, explanation, practice, and distortion-adaptation phases (Figure 1f). The practice and distortion adaptation phases were repeated twice. Each distortion-adaptation phase was carried out with time-locked or continuous classification in a random order using the non-personalized decoder which was calibrated with all data in the decoder-calibration phase recorded from the first two groups.

Single-trial procedure In both decoder-calibration and distortion-adaptation phases, each trial consisted of three times an arm reaching movement followed by two questions. Subjects started with their right hand on their belly holding a tennis ball. Three semitransparent spheres (blue, red, and green) and a red cross were displayed for each trial. Subjects were instructed to reach the first sphere (blue) to the right with the tennis ball and to remain inside at least 1 s to validate this first step. The validation progress was indicated in a gray circle, which became fully white once validated. Subjects then performed the avatar's arm reaching movement to the last sphere (green) while smoothly passing through the second sphere (red). The green sphere moved along a circular trajectory with a radius of 0.35 m. The distortion that helps reaching the green sphere (Figure 1b) was activated when the avatar's hand was located within the red sphere. The distortion function (attraction well [28], Section 2.3) was centered on the green target and expanded to the center of the red target (the same radius as the trajectory). Subjects had to stay inside the green target for at least 4 seconds to complete a trial. They were instructed to fixate their gaze on the red cross placed in front of them while doing the movement. If the gaze was not fixed on the red cross for 0.5s, the trial restarted after showing a warning message to subjects.

After each reaching movement, participants answered to two yes/no questions by controlling a cursor; "`I felt that the virtual body moved exactly like me`", and "`It felt that the virtual body was my own body.`". The first question indicates the subjective experience on conscious perception of the distorted avatar's arm reaching movement (perception of distortion, PoD) [34], and the second question indicates the presence of a BiE [1, 3]. After answering these questions, the full virtual scene reappeared at their initial position and the next trial started.

2.3. Attraction well

The distortion we used is designed to help participants reach and follow a moving target [1], and an excessive distortion is known to induce a BiE [4]. The avatar's hand was first attracted towards the target until it reached the outer boundary of the moving target (i.e. a sphere slightly bigger than a tennis ball). Once the virtual hand was inside the moving target, the attraction was then progressively reduced to zero until the avatar's hand arrived at the center of the target.

In our implementation, the distortion function started at the green sphere and extended towards the red one, following the trajectory. Please note that the green sphere's path aligned precisely with the red sphere's position. To facilitate tracking a vertically moving green sphere with one hand, we calibrated the position of the red sphere for each subject. This calibration ensured that subjects did not have to fully extend their arms as the red sphere's position never exceeded 80% of their arm length from the shoulder position.

The magnitude of distortion was controlled based on the distance D between the 3D position of subject's hand $\vec{P}_{real}$ and the 3D position of moving target $\vec{P}_{target}$ of radius R, by the following equations; $d = \frac{D}{d_{range}}$ and $r = \frac{R}{d_{range}}$ where d_{range} is the distance range of the attraction force centered on the moving target.

The distortion magnitude was expressed as a function of the normalized distance d (Figure 1b, d). For $d > 1$, no distortion occurred, hence the virtual hand position was identical to the real hand position. An attraction was enforced whenever $d < 1$ thereby bringing the avatar hand closer to the target compared to the real hand.

The maximum magnitude of the attraction force was denoted as G. Then:

$$f(d) = \begin{cases} G \times (-2 \times (\frac{d}{r})^3 + 3 \times (\frac{d}{r})^2)) & \text{d}\in [0,\text{r}] \\ G \times (2 \times (\frac{(d-r)}{(1-r)})^3 - 3 \times (\frac{(d-r)}{(1-r)})^2 + 1) & \text{d}\in [\text{r},1] \end{cases} \quad (1)$$

Given the distortion value provided by the attraction profile $f(d)$, an attraction coefficient was computed $1/(1 + f(d))$ to build the distorted hand position $\vec{P}_{distorted}$, shown to subjects, from the knowledge of the current positions of the mobile target $\vec{P}_{target}$ and the real hand $\vec{P}_{real}$. Then:

$$\vec{P}_{distorted} = \vec{P}_{target} + (\frac{1}{1 + f(d)}) \times (\vec{P}_{real} - \vec{P}_{target}) \quad (2)$$

The magnitude of distortion $f(d)$ being always positive, equation 2 ensured that the distorted hand position $\vec{P}_{distorted}$ always lied in-between the current target position $\vec{P}_{target}$ and the real hand position $\vec{P}_{real}$. Both the real and distorted positions coincided for the boundaries $[0, 1]$ of the normalized distance d. The distortion was tuned based on R, d_{range}, and G (referred to as the "distortion gain"). Based on the previous study [1], the following discrete distortion gains were used in the distortion-adaptation phase: (0, 0.25, 0.5, 0.75, 1, 1.25, 1.5, 1.75, 2, 2.25, 2.5, 2.75, 3, 4, 5, 7, 10). The last value covered

the largest possible magnitude of distortion due to the limited field of view of the VR display.

2.4. EEG signal processing

EEG acquisition We recorded 32 EEG and 3 electrooculogram (EOG) signals throughout the experiment at 512 Hz via three synchronized g.USBAmps (g.tec medical technologies, Austria). EEG active electrodes were located at AF3, AF4, F3, F1, Fz, F2, F4, FC3, FC1, FCz, FC2, FC4, C3, C1, Cz, C2, C4, CP3, CP1, CPz, CP2, CP4, P3, P1, Pz, P2, P4, PO3, POz, PO4, O1, O2 (10/10 international system), while the 3 EOG channels were placed above the nasion and below the outer canthi of the both eyes, forming a triangle. The ground electrode was placed on the forehead (AFz) and the reference electrode was on the left earlobe. The EEG and EOG signals were notch filtered at 50 Hz to eliminate the power noise. To reduce signal contamination, subjects were asked to stare at the cross and hold their heads still when reaching the targets. If the movements of the eyes or the neck were above a certain threshold, the trial was restarted to ensure the quality of the recorded signals.

Before the experiment, participants underwent 90 s of recording in which they were asked to perform three different kinds of eye movement, 30 s each; clockwise and counter-clockwise rolling of eyeballs, vertical and horizontal eye movements and repeated eye blinks. These data were subsequently used to compute coefficients to linearly remove EOG artifacts from EEG signals based on the autocovariance matrix of EEG and EOG signals [35, 36].

EEG preprocessing EEG signals were band-pass filtered with a 4th order Butterworth filter with cutoff frequencies of [1 10] Hz. The signals were then segmented into epochs with a time window of [0.2 0.6] s relative to when the participants passed through the red sphere for each trial.

Time-locked classification of ErrPs To build an ErrP decoder that monitors the presence or absence of ErrPs in real-time, we used only the data collected during the decoder-calibration phase. A personalized decoder was trained for participants in the first and second groups, while a non-personalized decoder was trained for the third group by accumulating all data in the first two groups' decoder-calibration phase. All EEG epochs were concatenated to build the non-personalized classifier.

To enhance the signal-to-noise ratio (SNR) of ErrPs for the subsequent classification analysis, we applied a spatial filter based on Canonical Correlation Analysis (CCA) [37, 38, 39, 26]. CCA-based spatial filters were linear transformations that maximize pairwise correlation between concatenated single-trial EEG epochs and averaged EEG epochs [40] (see [37] and Supp. Figure 1 for details). The CCA spatial filter transformed the averaged ErrPs into a subspace that contained different deflections. Only the first three components were kept for further processing as described in previous studies [25, 37].

We extracted EEG amplitudes resampled at 64 Hz and Welch's power spectral density between [4, 10] Hz with a step of 2 Hz as they have been shown to yield superior performance in other studies [25, 26, 41]. All computed features were concatenated and normalized within the range of [0, 1] via Min-Max normalization. From this feature vector $\mathbf{x}$, we computed the posterior probability of distortion $p(distortion|\mathbf{x})$ using diagonal linear discriminant analysis:

$$p(distortion|\mathbf{x}) = \frac{1}{1 + \exp^{-(\mathbf{w}'\mathbf{x}+b)}} \tag{3}$$

where, $\mathbf{w}$ and b are the parameters of the diagonal LDA.

For the first and third groups, in which a decoder was deployed to perform time-locked classification during distortion-adaptation phase, we used the theoretical decision threshold for binary classification, i.e. 0.5. Leave-one run-out cross validation was performed to validate the classification performance of the decoder-calibration phase for the first group.

Continuous classification of ErrPs For the second group that underwent the distortion-adaptation phase with a personalized decoder for continuous classification, the decoder was trained the same way as for the first group. In addition, we tuned the decision threshold. Leave-one run-out cross validation was performed to estimate the pseudo-continuous posterior probability at 32 Hz, i.e. from the onset to 0.6 s after reaching the green target. The maximum estimated posterior probability within a trial determined subjects' perception of BiEs. If the maximum estimated posterior probability was above the decision threshold, the decoder detected BiEs during continuous reaching movements. The optimal operating point, which yielded the minimum number of false predictions, of the Receiver Operating Characteristic (ROC) curve was determined as the decision threshold for the continuous classification.

For the third group, in which the non-personalized decoder was used during the distortion-adaptation phase, the optimal decision threshold for continuous classification was inferred for each participant based on the maximal posterior probabilities of the first four trials without distortion during the practice period (Figure 1f) [24]. We performed leave-one subject-out cross-validation to compute the pseudo-continuous probabilities of the data collected in the first two groups' distortion-adaptation phase while avoiding the use of individual decoder-calibration data. The averaged maximum posterior probability of the first four trials during the practice period and the individual optimal threshold were used to model the sigmoid function that inferred the optimal decision threshold.

Statistical analysis of ErrP decoding performance In the decoder-calibration phase, the classification performance of the time-locked and continuous classification was measured as the area under the curve (AUC) and was statistically evaluated by a two-sample t-test. In the distortion-adaptation phase, ErrP-BCI output was compared with the answers to the PoD and BiE questions. Classification performance was measured as balanced

classification accuracy, mean of true positive and true negative rate. Its chance level is 0.5. Paired t-test was used to evaluate the classification performance between the time-locked and continuous classification when using the non-personalized decoder, while a comparison of other pairs was performed by a two-sample t-test. All p-values were Bonferroni corrected.

2.5. Reinforcement Learning algorithm

In the present study, we used a reinforcement learning algorithm that had been developed and validated in our previous study [28] to determine the pseudo-optimal distortion value from a set of multiple options. Each of the available choices corresponded to a distinct level of distortion gain, and the agents' actions were met with positive or negative rewards, depending on the magnitude of the distortion introduced. This method enabled us to effectively identify the most suitable distortion level based on the user's implicit feedback, the ErrP-BCI output.

The reinforcement learning algorithm combined Upper-Confidence-Bound (UCB) exploration with the ϵ-greedy policy. Q-values were initialized to zero for all actions [42]. The convergence of the Q-values, representing the expected rewards for each action, was monitored to determine the optimal threshold.

To adapt to the dynamic nature of the problem, parameters such as the exploration ratio ϵ and the learning rate α decayed over time. The study carefully selected decay rates through a prior grid search. The algorithm also had termination conditions in place to avoid running indefinitely (15 unchanged iterations after the 35th trial and stopped if it reached 200 iterations). More details can be found in our previous study [28].

2.6. Psychometric function

We computed the PoD and BiE thresholds of each subject based on the answer to the first and second questions during the distortion-adaptation phase, respectively. We used a psychometric function [43, 44] to calculate each threshold (Supp. Figure 4). The PoD threshold is the magnitude of distortion in which subjects detected the distortion 50% of times, while the BiE threshold corresponded to an approximation of the minimum magnitude of distortion in which subjects rejected the virtual body as their body at 50% of times.

2.7. Statistical analysis of the thresholds

In order to evaluate whether PoD, BiE and RL thresholds were comparable, a one-way repeated measures ANOVA was performed for each decoding conditions, i.e., time-locked and continuous classification with personalized and non-personalized decoders.

3. Results

3.1. Electrophysiological analysis

We observed sequential negative, positive, and negative deflections after the onset of distortions in the decoder-calibration phase ($p < 0.05$, paired Wilcoxon signed-rank test followed by Benjamini-Hochberg false discovery correction (BHFDR), Figure 2a) [45, 46]. These deflections were present throughout the decoder-calibration phase (Supp. Figure 2). These deflections were strongly elicited from the parietal and central areas of the brain (Figure 2a). On the other hand, EEG potentials remained mostly flat around the onset without distortion. Similarly, in the distortion-adaptation phase, sequential deflections were observed when participants perceived distortion (Figure 2b) and when participants experienced BiE (Figure 2c), and these deflections were attenuated when they did not.

3.2. Decoding of ErrPs

In the decoder-calibration phase, the estimated posterior probability in the trials without distortion was lower than that with distortion (Figure 3a). The posterior probability increased progressively over the magnitude of distortion for both time-locked (Spearman r=0.72, p <0.001) and continuous classification (r=0.58, p <0.001). The AUC was 0.97 $\pm$ 0.007 (mean $\pm$ SE) for time-locked, and 0.89 $\pm$ 0.029 for continuous classification (Figure 3b). They were above the chance level (0.5), but the continuous classification performance was significantly lower than the time-locked classification performance (two-sample t-test, p =0.005, Figure 3b). Please note that our validation procedure, leave-one run-out cross validation, did not positively bias the ErrP-BCI classification performance (Supp. Figure 3).

Similarly to the decoder-calibration phase, the estimated posterior probability progressively increased over the magnitude of distortion in the distortion-adaptation phase for both time-locked (Spearman r=0.79, p <0.001) and continuous classification (r=0.62, p <0.001, Figure 4a and Supp. Figure 4). Despite its consistent trend over the magnitude of distortion, the probability was differentiated between time-locked and continuous classification, especially in trials with no or small distortion. Further, progressive increase in posterior probability was also observed when using the non-personalized decoder for both time-locked (r=0.62, p <0.001) and continuous classification (r=0.29, p <0.001, Figure 4b). The posterior probability range was smaller when using the non-personalized decoder compared to the corresponding classification approach using the personalized decoder.

In the distortion-adaptation phase, all four classification conditions outperformed the chance level as measured in balanced classification accuracy for both PoD (Figure 4c) and BiE questions (Figure 4d). For both questions, classification performance was highest for the time-locked classification with the personalized decoder. On the other hand, it was the lowest for the continuous classification with the non-personalized

	Personalized decoder		Non-personalized decoder	
	Time-locked	Continuous	Time-locked	Continuous
PoD threshold	1.20 ± 0.25	1.40 ± 0.30	1.36 ± 0.21	1.77 ± 0.41
BiE threshold	2.23 ± 0.70	2.84 ± 0.76	2.26 ± 0.74	2.18 ± 0.85
RL threshold	1.96 ± 0.19	1.94 ± 0.20	3.93 ± 0.85	2.95 ± 0.54
Number of trials	70 ± 6	77 ± 6	84 ± 12	75 ± 5

Table 1: PoD, BiE and RL thresholds and the number of trials performed in the distortion-adaptation phase for each decoding condition (mean ± SE).

decoder. When comparing ErrP-BCI outputs with the PoD question, the statistical differences were observed between the personalized and non-personalized decoder for both the time-locked (two-sample t-test, p=0.04) and continuous classification (two-sample t-test, p=0.02), and between time-locked and continuous classification when using the non-personalized decoder (paired t-test, p=0.03). There were no statistical differences between time-locked and continuous classification when using the personalized decoder (two-sample t-test, p=0.16). For the BiE question, the difference was observed between time-locked and continuous classification when using the personalized decoder (two-sample t-test, p=0.04) and between the personalized and non-personalized decoder for the time-locked classification (two-sample t-test, p=0.04). On the other hand, no differences were observed between time-locked and continuous classification when using the non-personalized decoder (paired t-test, p=1.0) and between the personalized and non-personalized decoder for continuous classification (two-sample t-test, p=0.30).

3.3. Behavioral and Reinforcement learning results

The PoD and BiE rates progressively increased along with the magnitude of distortion (Spearman r=0.68, p <0.001 for PoD, r=0.49, p <0.001 for BiE, Figure 5a). However, they showed slightly different modulations from each other. PoD rate showed a more rapid increase relative to BiE rate.

The RL threshold was between the PoD and BiE thresholds when using the personalized decoder (Figure 5b and Table 1). Statistical analysis did not reveal differences between the three thresholds (two one-way repeated measures ANOVAs, $F(2, 26) = 1.61, p = 0.219$ for time-locked, and $F(2, 22) = 2.52, p = 0.103$ for continuous classification). On the other hand, when the non-personalized decoder was used, the RL threshold was higher than the PoD and BiE thresholds (Figure 5c). The statistical analysis did not reveal significant differences between the three thresholds (two one-way repeated measures ANOVAs, $F(2, 20) = 3.22, p = 0.061$ for time-locked, and $F(2, 20) = 1.06, p = 0.364$ for continuous classification).

4. Discussion

We have presented a novel BCI-VR closed-loop system integrated in an immersive interactive system that allows seamless adjustment of the mapping between the users' actual movements and the one of their avatar for the benefit of interaction in VR. The present study demonstrated the possibility of adjusting the magnitude of distortion through an implicit ErrP-BCI feedback. The ErrP-BCI decoding output was exploited as reward signals to adjust the magnitude of distortion to perform the avatar's arm reaching movement while preserving the SoE, thus maintaining their virtual experiences. The proposed BCI-VR closed-loop system is beneficial for customizing the human-avatar mapping based on user's brain activity, which has been limited to users' explicit feedback to date. In order to compensate for the limited signal-to-noise ratio of the BCI output, we incorporated the RL algorithm to identify the optimal magnitude of distortion. The proposed approach successfully achieved the pseudo-optimal magnitude of distortion and demonstrated its ability to tune levels of assistance for each participant while avoiding degradation of virtual experiences due to BiEs.

Specifically, as shown in previous studies [1, 34, 47] and illustrated in Figure 5a, participants maintained a high level of embodiment even when they could perceive the distortion. In effect, we show that there are three distinct stages of cognitive processing before participants notice and then reject a movement distortion of their avatar. In the first stage, for very low distortions, they are not able to perceive the distortion. In the second stage, between the PoD and the BiE thresholds, participants are still experiencing a strong embodiment for their avatar despite being able to consciously evaluate that the avatar's arm reaching movement is distorted. In the third stage, beyond the BiE threshold, participants reject the distortion as an error of the system, provoking an ErrP that the BCI system can detect. The threshold computed by our BCI-RL approach successfully computed the pseudo-optimal threshold to be in between the PoD and the BiE thresholds when deploying the personalized ErrP decoder. Importantly, these RL thresholds were nearly identical to those obtained with explicit feedback (1.93 ± 0.23 [mean±SE]) [28] (Table 1). Thus, thanks to our tuned distortion magnitude, users performed the reaching task without affecting their experience of embodiment for their avatar.

As opposed to previous works that evaluated the user's brain response at given time points (e.g., after the executions of a movement by an avatar) [20, 21, 48], we performed continuous classification of ErrPs during avatar-based interactions and used the ErrP-BCI decoding outputs to customize the human-avatar mapping. Replacing time-locked by continuous classification of ErrPs is a challenge for BCI due to the uncertainty of EEG signals, but a necessary step for applying it to VR interaction, as users continuously interact with their embodied avatar. Although a previous work showed the customization of robot trajectories through continuous ErrP classification [26], their task did not involve varying magnitudes in erroneous interactions. A recent study [25] revealed the scalability of the ErrP-BCI decoding outputs over the magnitude of errors,

and posed the challenge of decoding ErrPs induced by small errors. Critically, our experimental protocol did not include trials with a small magnitude of distortions in the decoder-calibration phase. Nevertheless, our BCI-VR closed-loop system using a personalized decoder successfully classified trials with small distortions and customized the human-avatar mapping, allowing one to maintain embodiment for their avatar.

Furthermore, we also evaluated to what extent the decoder trained with multiple participants generalizes to a new group of participants (non-personalized decoder) [49, 50]. The decoding performance degraded both in time-locked and continuous classification compared to the personalized decoder (Figure 4c and d). The RL threshold obtained with the non-personalized decoder did not reveal significant differences from the PoE nor BiE threshold, while being higher than them. These RL thresholds were also higher than those identified with explicit feedback [28] (Table 1). Notably, when the non-personalized decoder was used, participants saved about 90 min as data collection to calibrate the personalized decoder was omitted. Thus, they were still able to receive implicit BCI feedback immediately after the practice to customize their human-avatar mapping. Although the non-personalized decoder showed degraded performance (Figure 4c and d), our analysis revealed a progressive increase in the output of the non-personalized decoder output for both time-locked and continuous classification over the magnitude of distortions, but limited to smaller ranges (Figure 4a and b). This suggests the importance of calibrating the decision threshold when deploying the non-personalized decoder for both time-locked and continuous classification and also the need to update the decoder to increase the range of posterior probabilities. These procedures may further improve precision of RL thresholds when using a non-personalized decoder.

One of the limitations of the present study is the relatively specific human-avatar mapping and BCI algorithms. For example, subjects were instructed to fix their gazes and head movements to preserve EEG signals from possible muscle contamination, and they performed repetitive reaching actions to collect enough data to build a personalized decoder and calibrate their interaction. In an ideal scenario, we expect participants to move freely without repetitive actions, while the BCI-VR closed-loop system implicitly calibrates their human-avatar mapping without the need for collecting data for building a personalized decoder.

In summary, this study demonstrated the possibility and showed the benefits of online adaptation of the human-avatar mapping during VR experiences, without asking explicitly or interrupting the interaction. Although the RL threshold obtained with a non-personalized decoder was not between PoD and BiE thresholds, the decoder may be adaptively updated in an experiment consisting of multiple sessions [25]. Thus, it would be crucially important to test our BCI-VR system over longitudinal sessions because one could speculate that users would increase their sensitivity to perceive visuo-proprioceptive conflicts and become more susceptible to BiE over time. Future studies may include use of the VR system over multiple sessions and evaluate their PoD, BiE and RL threshold, with the possibility to change over sessions while updating the decoder. With increasing involvement of full-body interaction in immersive VR

commercial products, BCI-VR systems would be beneficial for optimizing the human-avatar mapping, allowing to maintain an engaging avatar-based interaction and a compelling immersive experience while detecting when users notice a problem and seamlessly correcting it.

Acknowledgement

This work was supported by the Swiss National Science Foundation (project 'Immersive Embodied Interactions', 200020.178790), the Hasler Foundation, Switzerland, and by the Swiss National Center of Competence in Research in Robotics (NCCR).

ORCID IDs

Fumiaki Iwane: 0000-0002-9659-4127
Thibault Porssut:0000-0002-6691-1427
Olaf Blanke: 0000-0002-9745-3983
Ricardo Chavarriaga: 0000-0002-8879-2860
José del R. Millán: 0000-0001-5819-1522
Bruno Herbelin: 0000-0003-4570-5146
Ronan Boulic: 0000-0001-9176-6877

References

[1] Porssut T, Herbelin B and Boulic R 2019 Reconciling being in-control vs. being helped for the execution of complex movements in VR *IEEE Conference on Virtual Reality and 3D User Interfaces (VR)* (IEEE) pp 529–537 ISBN 978-1-72811-377-7

[2] Kilteni K, Groten R and Slater M 2012 The Sense of Embodiment in virtual reality *Presence: Teleoperators and Virtual Environments* **21** 373–387 ISSN 15313263

[3] Kokkinara E and Slater M 2014 Measuring the effects through time of the influence of visuomotor and visuotactile synchronous stimulation on a virtual body ownership illusion *Perception* **43** 43–58 ISSN 03010066

[4] Porssut T, Iwane F, Chavarriaga R, Blanke O, Millán J d R, Boulic R and Herbelin B 2023 EEG signature of breaks in embodiment in VR *PLOS ONE* **18** 1–13

[5] Falkenstein M, Hohnsbein J, Hoormann J and Blanke L 1991 Effects of crossmodal divided attention on late ERP components. II. Error processing in choice reaction tasks *Electroencephah)graphy and clinical Neurophysiology* **78** 447–455

[6] Gehring W J, Goss B, Coles M G H, Meyer D E and Donchin E 1993 A Neural System for Error Detection and Compensation *Psychological Science* **4** 385–390 ISSN 0956-7976

[7] Holroyd C B and Coles M G H 2002 The neural basis of human error processing: Reinforcement learning, dopamine, and the error-related negativity. *Psychol Rev* **109** 679–709

[8] Pezzetta R, Nicolardi V, Tidoni E and Aglioti S M 2018 Error, rather than its probability, elicits specific electrocortical signatures: A combined EEG-immersive virtual reality study of action observation *Journal of Neurophysiology* **120** 1107–1118 ISSN 15221598

[9] Spinelli G, Tieri G, Pavone E F and Aglioti S M 2018 Wronger than wrong: Graded mapping of the errors of an avatar in the performance monitoring system of the onlooker *NeuroImage* **167** 1–10 ISSN 10959572

[10] Pavone E F, Tieri G, Rizza G, Tidoni E, Grisoni L and Aglioti S M 2016 Embodying Others in Immersive Virtual Reality: Electro-Cortical Signatures of Monitoring the Errors in the Actions of an Avatar Seen from a First-Person Perspective *Journal of Neuroscience* **36** 268–279 ISSN 0270-6474

[11] Raz G, Gurevitch G, Vaknin T, Aazamy A, Gefen I, Grunstein S, Azouri G and Goldway N 2019 Electroencephalographic evidence for the involvement of mirror-neuron and error-monitoring related processes in virtual body ownership *NeuroImage* 116351 ISSN 10538119

[12] Padrao G, Gonzalez-Franco M, Sanchez-Vives M V, Slater M and Rodriguez-Fornells A 2016 Violating body movement semantics: Neural signatures of self-generated and external-generated errors *NeuroImage* **124** 147–156 ISSN 10959572

[13] Si-Mohammed H, Lopes-Dias C, Duarte M, Argelaguet F, Jeunet C, Casiez G, Müller-Putz G R, Lécuyer A and Scherer R 2020 Detecting system errors in virtual reality using eeg through error-related potentials *2020 IEEE Conference on Virtual Reality and 3D User Interfaces (VR)* pp 653–661

[14] Steinhauser R, Wirth R, Kunde W, Janczyk M and Steinhauser M 2018 Common mechanisms in error monitoring and action effect monitoring *Cognitive, Affective, & Behavioral Neuroscience* **18** 1159–1171

[15] Rabbitt P A 1966 Errors and error correction in choice-response tasks. *Journal of experimental psychology* **71** 264

[16] Chang A, Chen C C, Li H H and Li C S R 2014 Event-related potentials for post-error and post-conflict slowing *PloS one* **9** e99909

[17] Chavarriaga R and del R Millán J 2010 Learning From EEG Error-Related Potentials in Noninvasive Brain-Computer Interfaces *IEEE Transactions on Neural Systems and Rehabilitation Engineering* **18** 381–388 ISSN 1534-4320

[18] Ferrez P and del R Millán J 2008 Error-Related EEG Potentials Generated During Simulated Brain–Computer Interaction *IEEE Transactions on Biomedical Engineering* **55** 923–929 ISSN 0018-9294

[19] Ferrez P W and Millán J d R 2008 Error-related EEG potentials generated during simulated brain–computer interaction *IEEE Transactions on Biomedical Engineering* **55** 923–929

[20] Iturrate I, Chavarriaga R, Montesano L, Minguez J and Millán J d R 2015 Teaching brain-machine interfaces as an alternative paradigm to neuroprosthetics control *Scientific Reports* **5** 13893 ISSN 2045-2322

[21] Salazar-Gomez A F, DelPreto J, Gil S, Guenther F H and Rus D 2017 Correcting robot mistakes in real time using EEG signals *IEEE International Conference on Robotics and Automation* pp 6570–6577

[22] Chavarriaga R, Sobolewski A and Millán J d R 2014 Errare machinale est: The use of error-related potentials in brain-machine interfaces *Frontiers in Neuroscience* **8** 208 ISSN 1662-453X

[23] Dias C L, Sburlea A I and Müller-Putz G R 2018 Masked and unmasked error-related potentials during continuous control and feedback *Journal of Neural Engineering* **15** 036031

[24] Lopes-Dias C, Sburlea A I, Breitegger K, Wyss D, Drescher H, Wildburger R and Müller-Putz G R 2021 Online asynchronous detection of error-related potentials in participants with a spinal cord injury using a generic classifier *Journal of Neural Engineering* **18** 046022 ISSN 1741-2552

[25] Iwane F, Sobolewski A, Chavarriaga R and Millán J d R 2023 Eeg error-related potentials encode magnitude of errors and individual perceptual thresholds *iScience* **26** ISSN 2589-0042

[26] Batzianoulis I, Iwane F, Wei S, Correia C G P R, Chavarriaga R, Millán J d R and Billard A 2021 Customizing skills for assistive robotic manipulators, an inverse reinforcement learning approach with error-related potentials *Communications Biology* **4** 1406 ISSN 2399-3642

[27] Iwane F, Billard A and Millán J d R 2023 Inferring individual evaluation criteria for reaching trajectories with obstacle avoidance from EEG signals *Scientific Reports* **13** 20163 ISSN 2045-2322

[28] Porssut T, Hou Y, Blanke O, Herbelin B and Boulic R 2022 Adapting virtual embodiment through

reinforcement learning *IEEE Transactions on Visualization and Computer Graphics* **28** 3193–3205

[29] Jauregui D A G, Argelaguet F, Olivier A H, Marchal M, Multon F and Lecuyer A 2014 Toward 'pseudo-haptic avatars': Modifying the visual animation of self-avatar can simulate the perception of weight lifting *IEEE Transactions on Visualization and Computer Graphics* **20** 654–661 ISSN 10772626

[30] Azmandian M, Hancock M, Benko H, Ofek E and Wilson A D 2016 Haptic retargeting: Dynamic repurposing of passive haptics for enhanced virtual reality experiences *Conference on Human Factors in Computing Systems - Proceedings* pp 1968–1979 ISBN 978-1-4503-3362-7

[31] Burns E, Razzaque S and Whitton M 2007 MACBETH: Management of avatar conflict by employment of a technique hybrid *International Journal of Virtual Reality* **6** 11–20

[32] Bowman D A and Hodges L F 1997 An evaluation of techniques for grabbing and manipulating remote objects in immersive virtual environments *Proceedings of the 1997 symposium on Interactive 3D graphics* pp 35–ff

[33] Porssut T, Blanke O, Herbelin B and Boulic R 2022 Reaching articular limits can negatively impact embodiment in virtual reality *Plos one* **17** e0255554

[34] Galvan Debarba H, Boulic R, Salomon R, Blanke O and Herbelin B 2018 Self-attribution of distorted reaching movements in immersive virtual reality *Computers and Graphics (Pergamon)* **76** 142–152 ISSN 00978493

[35] Schlögl A, Keinrath C, Zimmermann D, Scherer R, Leeb R and Pfurtscheller G 2007 A fully automated correction method of EOG artifacts in EEG recordings *Clinical Neurophysiology* **118** 98 – 104 ISSN 1388-2457

[36] Iwane F, Iturrate I, Chavarriaga R and Millán J d R 2021 Invariability of eeg error-related potentials during continuous feedback protocols elicited by erroneous actions at predicted or unpredicted states *Journal of Neural Engineering* **18** 046044 ISSN 1741-2552

[37] Spüler M, Walter A, Rosenstiel W and Bogdan M 2014 Spatial Filtering Based on Canonical Correlation Analysis for Classification of Evoked or Event-Related Potentials in EEG Data *IEEE Transactions on Neural Systems and Rehabilitation Engineering* **22** 1097–1103 ISSN 1534-4320

[38] Iwane F, Chavarriaga R, Iturrate I and Millán J d R 2016 Spatial filters yield stable features for error-related potentials across conditions *2016 IEEE International Conference on Systems, Man, and Cybernetics* pp 661–666

[39] Spüler M 2017 Spatial filtering of EEG as a regression problem *7th Graz Brain-Computer Interface Conference*

[40] Hotelling H 1936 Relations between two sets of variates *Biometrika* **28** 321–377

[41] Zhang H, Chavarriaga R, Khaliliardali Z, Gheorghe L, Iturrate I and d R Millán J 2015 Eeg-based decoding of error-related brain activity in a real-world driving task *Journal of Neural Engineering* **12** 066028

[42] Sutton R S, Barto A G *et al.* 1998 *Introduction to reinforcement learning* vol 135 (MIT press Cambridge)

[43] Lecuyer A, Coquillart S, Kheddar A, Richard P and Coiffet P 2000 Pseudo-haptic feedback: can isometric input devices simulate force feedback? *Proceedings IEEE Virtual Reality* pp 83–90 ISBN 0-7695-0478-7 ISSN 1087-8270

[44] Klein S A 2001 Measuring, estimating, and understanding the psychometric function: A commentary *Perception & Psychophysics* **63** 1421–1455 ISSN 1532-5962

[45] Hajcak G, McDonald N and Simons R F 2003 To err is autonomic: Error-related brain potentials, ANS activity, and post-error compensatory behavior *Psychophysiology* **40** 895–903

[46] Gehring W, Liu Y, Orr J and Carp J 2012 The error-related negativity (ERN/Ne) *The Oxford Handbook of Event-Related Potential Components*

[47] Debarba H G, Perrin S and Boulic R 2018 Perception of Redirected Pointing Precision in Immersive Virtual Reality *IEEE Virtual Reality IEEE IEEE Virtual Reality*

[48] Ehrlich S K and Cheng G 2018 Human-agent co-adaptation using error-related potentials *Journal*

of Neural Engineering **15** 066014 ISSN 1741-2552

[49] Lopes-Dias C, Sburlea A I and Müller-Putz G R 2020 A generic error-related potential classifier offers a comparable performance to a personalized classifier *2020 42nd Annual International Conference of the IEEE Engineering in Medicine & Biology Society (EMBC)* 2020 42nd Annual International Conference of the IEEE Engineering in Medicine & Biology Society (EMBC) pp 2995–2998 ISSN 2694-0604

[50] Bhattacharyya S, Konar A, Tibarewala D N and Hayashibe M 2017 A generic transferable eeg decoder for online detection of error potential in target selection *Frontiers in Neuroscience* **11** ISSN 1662-453X original Research

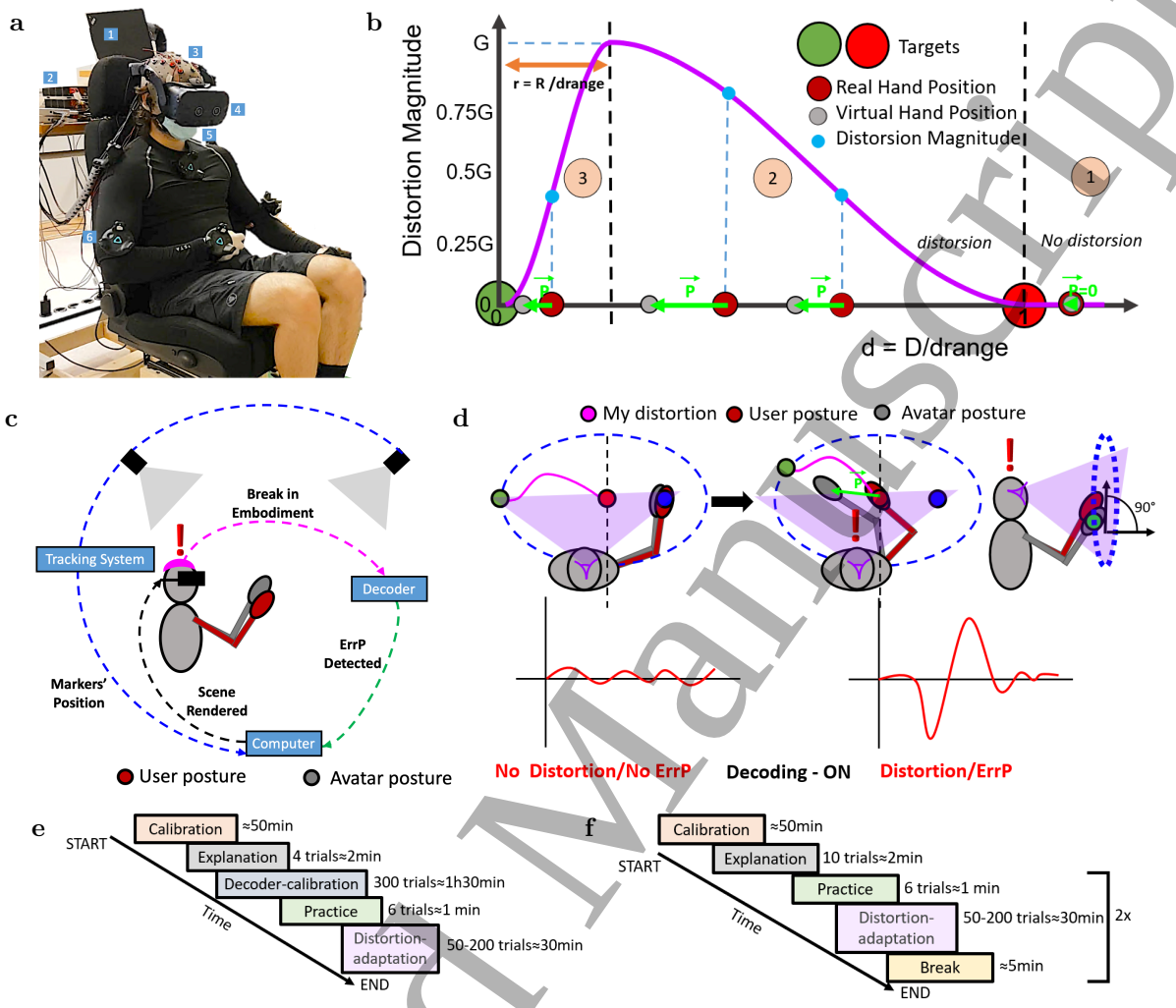

Figure 1: Protocol Overview. **a**, Setup of the experiment. 1). Computer connected to the EEG amplifier, 2). EEG amplifier, 3). EEG cap and electrodes, 4). HMD (HTC Vive), 5). Mask and gloves were worn during the experiment due to the COVID-19 safety regulations and 6). Motion tracker (HTC Vive tracker). **b**, Overview of the well-shaped distortion function (attraction well). No distortion was applied when d is greater than 1 (region 1). When d is below 1, the virtual hand attracted to the target. The magnitude of attraction increased inverse proportion of d from 1 to r (region 2). The attraction diminished to zero as d decreases from r to 0 (region 3). **c**, Participants were immersed to VR environment by using tracking system and head mounted display, while recording EEG signals. During the distortion-adaptation phase, online detection of ErrPs were performed to infer occurrence of BiE. **d**, Each trial consisted of the the two sequential reaching movements; i). from belly to the blue sphere, ii). from blue sphere to green sphere while passing through the red sphere. The distortion was induced when passing through the red sphere to induce BiE. **e**, Main phases of the first and second groups. Time-locked classification was performed during the distortion-adaptation phase for the first group and the continuous classification was performed for the second group . **f**, Main phases timeline of the third group. Each distortion-adaptation phase performed time-locked or continuous classification in a random order.

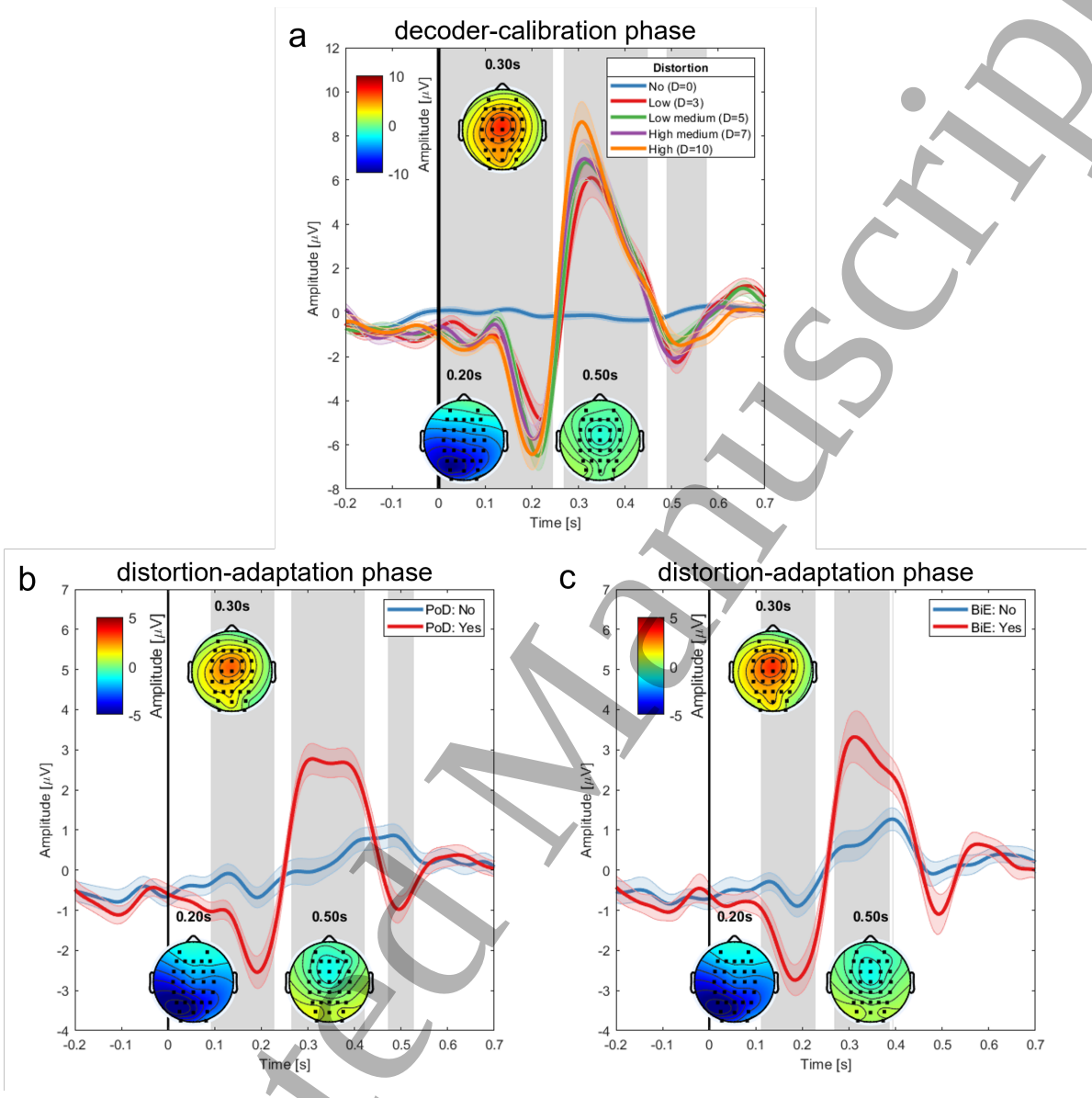

Figure 2: Grand-averaged EEG potentials at Cz electrode. **a**, Grand averaged signals of Cz channel with respect to the onset of trials (the vertical black line, t=0) with a non-causal band-pass filter in decoder-calibration phase. Each colored line and shaded area correspond to different magnitudes of distortion (mean ± SE). The gray-shaded areas represent the time samples in which significant differences were observed between the trials without distortion (D = 0) and those with distortion (D = 3, 5, 7, 10, paired Wilcoxon signed-rank test followed by BHFDR, $\alpha < 0.05$). Insets represent topographical representations of each deflection at 0.20, 0.30 and 0.50 s. **b**, Grand averaged signals of Cz channel in distortion-adaptation phase. Each colored line corresponds to the answer to the perception of distortion (PoD) question. The gray-shaded areas represent the time samples with significant differences between each answer. **c**, Grand averaged signals of Cz channel in distoation-adaptation phase. Each colored line corresponds to the answer to the break-in-embodiment (BiE) question.

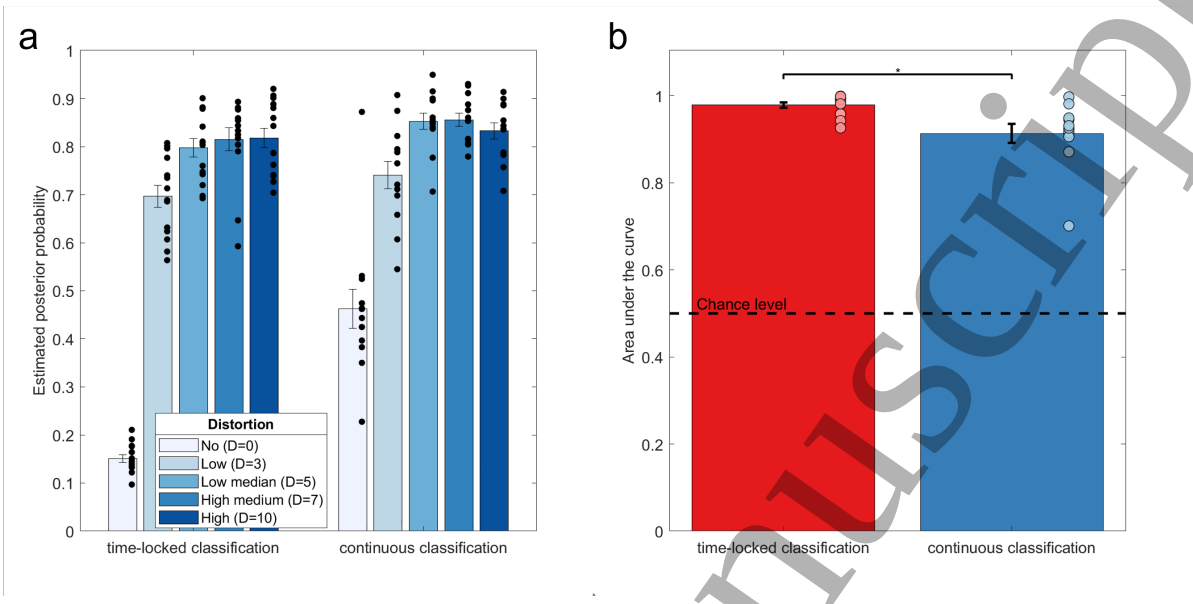

Figure 3: Decoding results of ErrPs in the decoder-calibration phase. **a**, Estimated posterior probability while validating the personalized decoder for each magnitude of distortion in the time-locked and continuous classification (mean ± SE). The decoder was trained to differentiate between trials with and without distortion. Each black dot corresponds to a participant. **b**, The area under the curve (AUC) of the time-locked and continuous classification (mean ± SE). The horizontal black dashed line indicates their chance level (0.5). Each dot corresponds to a participant. AUC was higher in the time-locked classification than in the continuous classification (two-sample t-test, p=0.005).

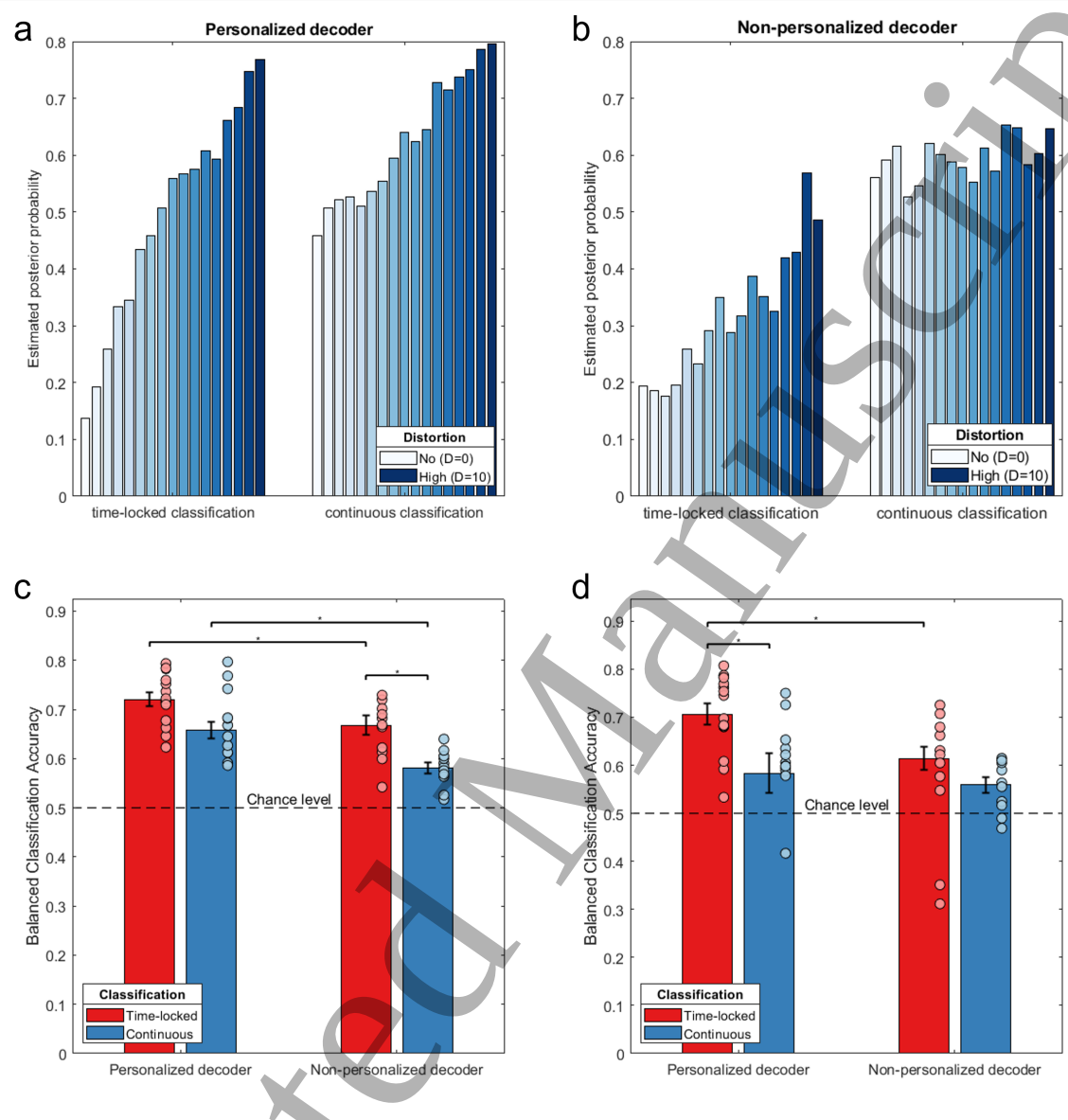

Figure 4: Decoding results of ErrPs in the distortion-adaptation phase. **a**, Estimated posterior probability for all 17 magnitudes of distortion in the distortion-adaptation phase for the time-locked and continuous classification when using the personalized decoder.**b**, Estimated posterior probability when using the non-personalized decoder. **c**, Balanced classification accuracy compared to the PoD answer for time-locked and continuous classification when using the personalized and the non-personalized decoder (mean ± SE). The horizontal black dashed line indicates the chance level, 0.5. Each dot corresponds to a participant for each decoding condition. Statistical analysis revealed significant differences between the personalized and non-personalized decoder for both the time-locked (two-sample t-test, p=0.04) and continuous classification (p=0.02), and between time-locked and continuous classification when using the non-personalized decoder (paired t-test, p=0.03). **d**, Balanced classification accuracy compared to the BiE answer (mean ± SE). Significant differences were observed between time-locked and continuous classification when using the personalized decoder (two-sample t-test, p=0.04) and between the personalized and non-personalized decoder for time-locked classification (p=0.04).

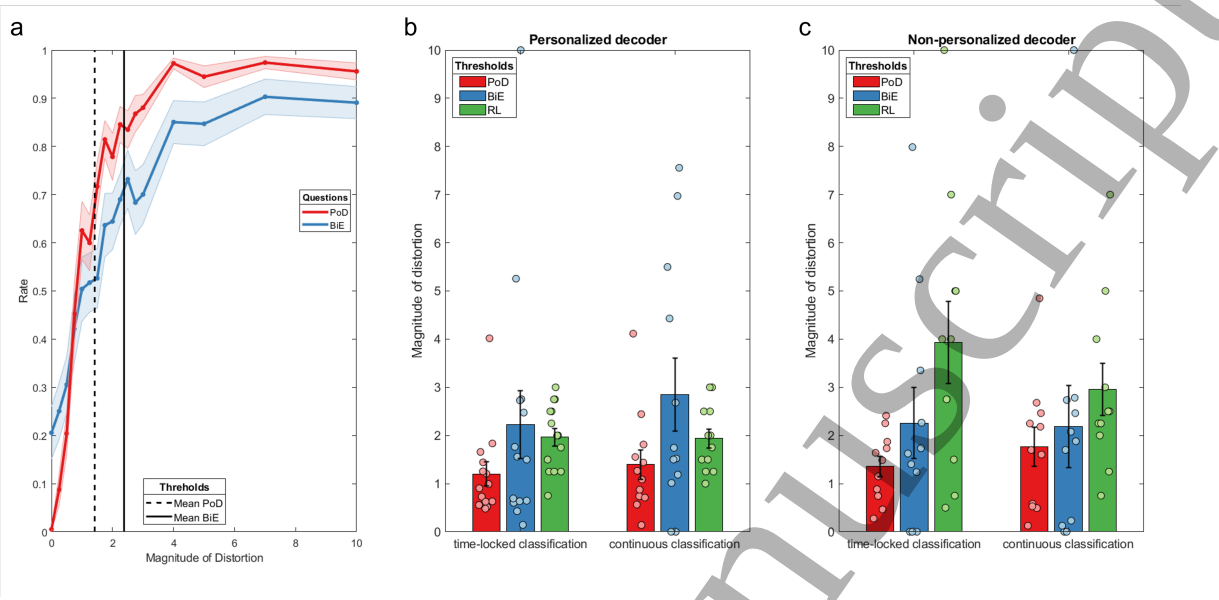

Figure 5: Behavioral results and comparison of the PoD, BiE and RL thresholds. **a**, Behavioral answer to the perception of distortion (PoD) and break-in-embodiment (BiE) questions for each magnitude of distortion. Each colored line and shaded areas represents the answer to each question (mean ± SE). The black dashed vertical line represents the mean PoD threshold, while the solid black vertical line indicates the mean BiE threshold. **b**. PoD, BiE and RL thresholds for time-locked and continuous classification when using the personalized decoder. Each bar corresponds to the PoD (red), BiE (blue), and RL threholds (green). Each dot corresponds to a participant. No statistical differences were observed between the three thresholds (two one-way repeated measures ANOVAs, $F(2, 26) = 1.61, p = 0.219$ for time-lock, and $F(2, 22) = 2.52, p = 0.103$ for continuous classification). **c**. PoD, BiE and RL thresholds for time-locked and continuous classification when using the non-personalized decoder. Similar to the case using the personalized decoder, No statistical differences were observed between the three thresholds (two one-way repeated measures ANOVAs, $F(2, 20) = 3.22, p = 0.061$ for time-lock, and $F(2, 20) = 1.06, p = 0.364$ for continuous classification).